Aparicio Esteve, E., Raes, W., Stevens, N., Ureña, J. & Hernández, A. 2022, "Experimental Evaluation of a Machine Learning-Based RSS Localization Method Using Gaussian Processes and a Quadrant Photodiode", Journal of Lightwave Technology, vol. 40, no. 19, pp. 6388-6396.

Available at http://dx.doi.org/10.1109/JLT.2022.3198009

Experimental Evaluation of a Machine Learning-Based RSS Localization Method Using Gaussian Processes and a Quadrant Photodiode

Elena Aparicio-Esteve, Willem Raes, Nobby Stevens, Jesús Ureña, Álvaro Hernández

***Abstract*—The research interest on indoor Location-Based Services (LBS) has increased during the last years, especially using LED lighting, since they can deal with the dual functionality of lighting and localization with centimetric accuracy. There are several positioning approaches using lateration and angular methods. These methods typically rely on the physical model to deal with the multipath effect, environmental fluctuations, calibration of the optical setup, etc. A recent approach is the use of Machine Learning (ML) techniques. ML techniques provide accurate location estimates based on observed data without requiring the underlying physical model to be described. This work proposes an optical indoor local positioning system based on multiple LEDs and a quadrant photodiode plus an aperture. Different frequencies are used to allow the simultaneous emission of all transmitted signals and their processing at the receiver. For that purpose, two algorithms are developed. First, a triangulation algorithm based on Angle of Arrival (AoA) measurements, which uses the Received Signal Strength (RSS) values from every LED on each quadrant to determine the image points projected from each emitter on the receiver and, then, implements a Least Squares Estimator (LSE) and trigonometric considerations to estimate the receiver's position. Secondly, the performance of a data-driven approach using Gaussian Processes is evaluated. The proposals have been experimentally validated in an area of $3 \times 3\,\mathrm{m}^2$ and a height of 1.3 m (distance from transmitters to receiver). The experimental tests achieve p50 and p95 2D absolute errors below 9.38 cm and 21.94 cm for the AoA-based triangulation algorithm, and 3.62 cm and 16.65 cm for the Gaussian Processes.**

***Index Terms*—Quadrant Photodiode, Visible Light Positioning, Gaussian Processes.**

I. Introduction

The demand for accurate and affordable positioning systems has increased significantly with the development of various Location-Based Services (LBS), where users are offered a range of applications based on their position in a specific area [1]. These services introduce a new challenge in determining the precise location of people, robots, or any other device, not only outdoors, where Global Navigation Satellite Systems (GNSS) offer a viable solution, but also indoors, where there is a lack of GNSS coverage and, therefore, accuracy in indoor environments, particularly within buildings with numerous floors, thick walls, and locations far from windows [2]. Multiple indoor localization technologies have been developed to overcome those weaknesses, based on acoustic [3], mechanical [4], radio-frequency [5], and optical [6] signals, among others.

In particular, the use of optical positioning systems (visible light, VLP [7] or infrared light, IRLP [8]) is a feasible option that has begun to expand as a result of their low cost, long lifetime and broad distribution in the majority of buildings, homes and indoor spaces [9]. Both VLP and IRLP typically employ multiple Light Emitting Diodes (LEDs) as transmitters, and a camera, a single photodiode or an array of photodiodes as receiver. Previous works that use arrays of photodiodes can be classified into three broad categories [10]: aperture-based, lens-based, and tilted photodiode-based designs. Those based on tilted photodiodes or prisms [11] [12] are larger in size and number of photodiodes, and typically offer limited resolution in AoA measurement (sometimes quantified ranges of angles). Higher resolution in AoA estimation is possible with aperture-based designs using quadrant photodiodes, but with Field of View (FoV) limitations [13]. The use of a Quadrant Photodiode Angular Diversity Aperture (QADA) is highlighted due to its better angular diversity [14]. Finally, Position Sensitive Detectors (PSD) are frequently used in lens-based systems (e.g., with a hemispherical lens) to provide higher FoV, achieving higher refresh rates than cameras, but they have smaller bandwidths than QADA photodiodes [15]. They must also take into account how the lens affects the photodiode to achieve a high accuracy [16].

There are several approaches to obtain the indoor coordinates based on VLP, such as Times of Flight (ToF), Received Signal Strength (RSS), and Angles of Arrival (AoA). These techniques rely on lateration and angulation methods to finally estimate the position of the mobile node. Positioning using RSS measurements implies taking into account the reflections of light on surfaces and the consequent multipath effect, as well as the transmitter radiation pattern and the transmitter tilt

This work was supported in part by the European Science Foundation under COST Action CA19111 - NEWFOCUS under the form of a Short-term scientific missions (STSM), with the University of Alcalá (Spain) as Home Institution and KU Leuven (Belgium) as Host Institution, in part by the Spanish Ministry of Science and Innovation under Project RTI2018-095168-BC51, and in part by the University of Alcalá (Spain) under the Mobility Grant for Research Staff in Training. The authors gratefully acknowledge the Internal Funds KU Leuven Start-up Grant that made this research possible.

Elena Aparicio-Esteve is with the Electronics Department, University of Alcalá, 28805 Alcalá de Henares, Spain and with the Department of Electrical Engineering, KU Leuven, 3000 Leuven, Belgium (e-mail: elena.aparicio@uah.es). Willem Raes and Nobby Stevens are with the Department of Electrical Engineering, KU Leuven, 3000 Leuven, Belgium (e-mail: willem.raes@kuleuven.be; nobby.stevens@kuleuven.be). Jesús Ureña and Álvaro Hernández are with the Electronics Department, University of Alcalá, 28805 Alcalá de Henares, Spain (e-mail: jesus.urena@uah.es; alvaro.hernandez@uah.es).

angles, which increase the complexity of the positioning algorithm [17]. It is worth noting that ToF measurements require to deal with the velocity of light and, consequently, small time estimation errors in the range of 1 ns can lead to a 30 cm error in position [18]. Finally, the AoA-based positioning algorithms are robust against source and environmental fluctuations (dust, fumes, etc.), it is not necessary to have a synchronisation between transmitters, although an accurate calibration of the optical setup (i.e. intrinsic parameters of the optical receiver) may be required [19].

A recent approach to further improve the performance of VLP schemes is the use of Machine Learning (ML) techniques [20] [21] [22]. The main advantage of these data-driven methods is that they can provide reliable location estimates based on observed data, without having to accurately describe the underlying physical model. In general, there is no need to have prior information on the physical model since it is embedded in the training set; however, including domain-specific knowledge can improve and simplify the model selection and training process. Apart from the straightforward position estimation, ML methods have been successfully applied in the context of localization using both supervised and unsupervised approaches for many other problems e.g., Non-Line-of-Sight (NLOS) detection and mitigation [23] [24]. In addition, ML methods also offer the ability to easily fuse input data from multiple types of sensors and other available information sources.

Table I provides a comparison between previous VLP works. The parameters to be compared in the literature are: the number of LEDs required in the implementation; the type of receiver, including any additional non-optical hardware; the coverage area at which the proposed system can operate and the position accuracy achieved inside it; and, finally, the implemented positioning technique. It is worth noting that a large variety of experimental situations can be found, based on a low number of LEDs. Some works operate in a few centimetres [12], [25], [26], whereas others provide solutions for several meters [27], [28], [29] (although these last ones are simulations). Regarding the type of receiver, all the works require at least four photodiodes (PDs) to achieve positioning accuracies below 10 cm. Finally, the implemented positioning techniques are mainly related to ML techniques [27], [25], [26], although some of them use fingerprinting (FP) [28] or Cramer-Rao Bound (CRB) and Gauss-Newton (GN) approximations [29].

This work focuses on the design and experimental validation of a VLP system based on a set of four transmitting LEDs (beacons) placed at known positions. A quadrant photodiode (QP) with a square aperture is used as receiver. The VLP system relies on the reception and further processing of different simultaneously emitted and modulated signals by the aforementioned LEDs, in order to provide position estimates. The system processes the received signals to estimate the RSS value from each LED at the receiver. Based on these values, two algorithms are evaluated in this work. Firstly, an AoA-based triangulation approach is presented, where, after the estimation of the RSS values, the 2D projections from the beacons on the QP are estimated, and, then, the pose of the receiver is derived. Secondly, a data-driven approach using Gaussian Process (GP) regression [30] is evaluated. For this strategy, the intensities received from the four quadrants of the QP are fed into an autoencoder model for dimensionality reduction and feature extraction, and the resulting features are employed as inputs for the GP model, which finally delivers positioning outputs. A real prototype has been assembled to successfully validate both approaches in an experimental setup with a 1.3 m distance between the beacons' and receiver's planes.

The rest of the manuscript is organized as follows: Section II provides an overview of the proposed system; Section III describes the applied AoA-based triangulation and Gaussian Process algorithms; Section IV shows some experimental results obtained in the proposed setup; and, finally, conclusions are discussed in Section V.

II. Global Proposed System

The proposed visible light positioning system is based on four visible light LED emitters located at known positions in the ceiling, covering a volume large enough for the receiver to detect all transmissions and determine its own position. If a larger system is needed, the proposed system can be simply extended by increasing the number of LEDs deployed in the environment. Note that in order to estimate the position of the receiver using a triangulation algorithm, the coverage from at least 3 LEDs is needed. A more robust system can be achieved by increasing the number of LEDs. A general diagram of the VLP system is presented in Fig. 1. In this proposal, two independent coordinate systems are considered: the Cartesian coordinates in the global coordinate system are denoted as x, y, z, with the origin at the corner of the room, and the local 2D coordinates of the quadrant photoreceiver are represented as x_r, y_r, with the origin at the centre of the receiver. The receiver's pose is denoted as (x, y, z, γ), where γ is the receiver's rotation angle around the Z axis. No rotation around the X or Y axes is considered.

Note that, since the positioning algorithm relies on the receiver identifying the different transmissions coming from the four LEDs, a medium access scheme has to be employed. In this case Frequency Division Multiple Access (FDMA) technique is used, where each LED i transmits a power-switched waveform at an unambiguous fundamental frequency f_i. The receiver can recognise these frequencies by applying the Fast Fourier Transform (FFT).

In Fig. 2, the Position Dilution of Precision (PDOP) [31] details the behaviour of the proposed VLP system at plane $z = 0$ m in the analysed scenario. The projections of the transmitters in the XY plane are denoted with black crosses. The positions of the transmitters ($x_{t,i}$, $y_{t,i}$, $z_{t,i}$) are provided in Table II. It can be observed that the PDOP significantly increases at the corners of the test area in comparison with the centre of the room.

III. Proposed Algorithms

As can be observed in Figs. 1 and 3, the light passes through the aperture and illuminates the quadrant photoreceiver,

TABLE I
COMPARISON OF PREVIOUS VLPS SCHEMES.

Ref.	No. of LEDs	Test area (W L H) (m)	Type of receiver	Position accuracy (rMSE) (cm)	Positioning technique	Results
[12]	1	0,2 x 0,2 x 0,45	4 tilted PDs	2	AoA	Experimental
[25]	1	0,4 x 0,4 x 1	4 Si-PVC with barriers	3,08	AoA + Ridge Regresssion	Experimental
[26]	1	0,4 x 0,4 x 1	4 Si-PVC with barriers	2.99	AoA + 2 layer Neural Network	Experimental
[27]	4	5 x 5 x 2	8 PDs with apertures	10	AoA + Iterative ML estimator	Simulations
[28]	1	5 x 5 x 3	4 PDs	5	RSS + FP	Simulations
[29]	10-100	8 x 6 x 3	6 PDs	100-10	CRB + GN	Simulations

Silicon Photovoltaic Cells (Si-PVC)

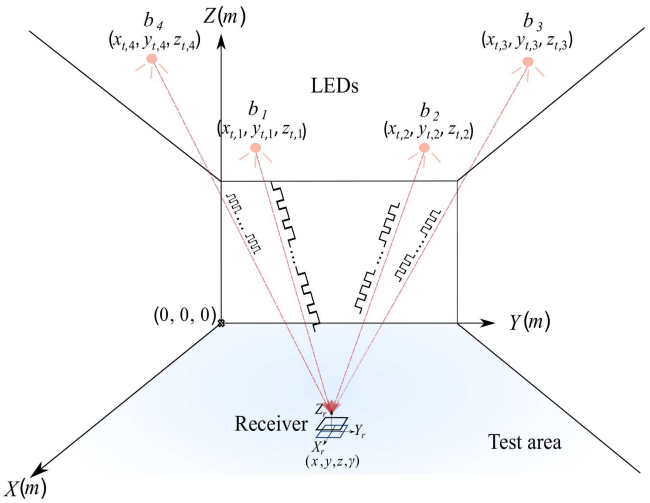

Fig. 1. Global overview of the proposed VLP system. Four LEDs placed in the ceiling of the room transmit a modulated signal (each LED at a different frequency) so that the receiver can distinguish their corresponding signal strength.

TABLE II
LEDS' COORDINATES CONSIDERED IN FIG. 2.

LED b_i	**Coordinates** $(x_{t,i}, y_{t,i}, z_{t,i})$
LED 1	(2.40 m, 0.60 m, 1.35 m)
LED 2	(1.05 m, 0.60 m, 1.35 m)
LED 3	(1.05 m, 2.40 m, 1.35 m)
LED 4	(2.40 m, 2.40 m, 1.35 m)

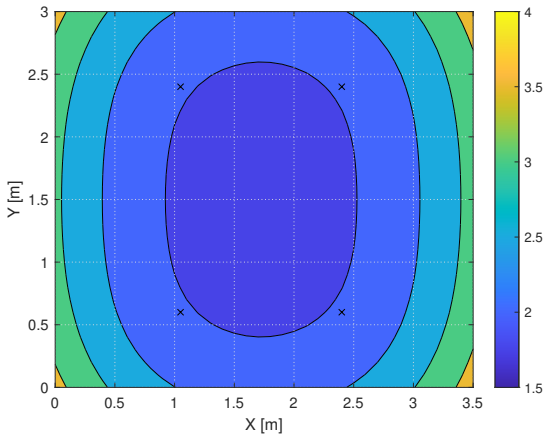

Fig. 2. PDOP of the proposed VLP system in the coverage area when the receiver is placed at plane $z = 0$ m. The projections of the transmitters at plane $z = 0$ m are represented with black crosses.

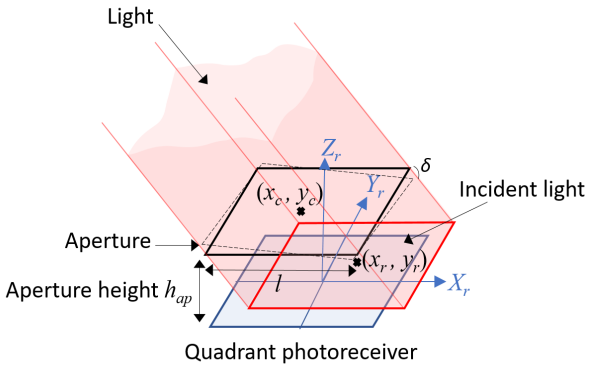

Fig. 3. Global overview of the quadrant photoreceiver with a square aperture. The incident light passes through the square aperture and illuminates the quadrant photoreceiver. The central point of incidence of the light (image point) is denoted as (x_r, y_r). The calibration parameters of the receiver's aperture are: height h_{ap}, length l, centre (x_c, y_c) and rotation δ.

thus generating four currents $i_j(t)$, one for each quadrant $j = \{1, 2, 3, 4\}$. These four signals are acquired and processed to obtain the RSS values from each LED. In order to identify the RSS value of each transmitter, the system performs the FFT of the received signal from each quadrant and, then, selects the corresponding value of the FFT output for each frequency of interest, while rejecting other undesired signals (ambient light, incoming sunlight and noise, etc.), and ensuring that the receiver circuit is not saturated. Note that these RSS-values are assumed to be proportional to the illuminated areas, as well as to the output voltage from each quadrant [14], [32]. In addition, in order to have a more robust system, the FFT is conducted over 5 periods of the signal to reduce spectral leakage.

From this point, two algorithms are evaluated. On one hand, we present an AoA-based triangulation algorithm that first uses the acquired RSS values to estimate the image points $(x_r, y_r)_i$ for each LED i and, then, estimates the receiver's position (x, y, z) and the rotation γ of the receiver in the Z axis, by using a Least Squares Estimator (LSE) and trigonometric considerations. In the second strategy we adopt two machine learning models, where one performs the feature extraction and the other estimates the receiver's 2D position (x, y). As the photoreceiver consists of four distinct quadrants, each quadrant generates an RSS-vector of four intensities linked to the power contributions of each transmitter on that quadrant. This results in an input dimensionality of 16 for the ML-models. In the first step of the data-driven strategy, an autoencoder [33] neural

network is used to lower the input dimensionality and to generate features that will be used as inputs for a GP, which in turn provides (x, y) location estimates.

A. AoA-based Triangulation Algorithm

We refer to the energy received at each frequency (the RSS values) as QD_j, one for each quadrant $j = \{1, 2, 3, 4\}$. These values can be combined to obtain the ratios (p_x, p_y) as:

$$p_x = \frac{QD_1 + QD_4}{QD_2 + QD_3} = \begin{cases} \frac{l/2+x_r}{l/2}, & -l/2 < x_r \leq 0 \\ \frac{l/2}{l/2-x_r}, & 0 < x_r \leq l/2 \end{cases} \quad (1)$$

$$p_y = \frac{QD_1 + QD_2}{QD_3 + QD_4} = \begin{cases} \frac{l/2+y_r}{l/2}, & -l/2 < y_r \leq 0 \\ \frac{l/2}{l/2-y_r}, & 0 < y_r \leq l/2 \end{cases} \quad (2)$$

The ratios p_x and p_y are used to estimate the image point (x_r, y_r) for each transmitter in the quadrant photodiode, as detailed in Eqs. (3) and (4).

$$x_r = \begin{cases} \frac{l}{2} \cdot \lambda \cdot (\delta \cdot (p_y - 1) + (p_x - 1)) + x_c, \forall p_x < 1; \forall p_y < 1 \\ \frac{l}{2} \cdot \lambda \cdot (\delta \cdot (p_y - 1) + (1 - \frac{1}{p_x})) + x_c, \forall p_x \geq 1; \forall p_y < 1 \\ \frac{l}{2} \cdot \lambda \cdot (\delta \cdot (1 - \frac{1}{p_y}) + (p_x - 1)) + x_c, \forall p_x < 1; \forall p_y \geq 1 \\ \frac{l}{2} \cdot \lambda \cdot (\delta \cdot (1 - \frac{1}{p_y}) + (1 - \frac{1}{p_x})) + x_c, \forall p_x \geq 1; \forall p_y \geq 1 \end{cases} \quad (3)$$

$$y_r = \begin{cases} \frac{l}{2} \cdot \lambda \cdot (-\delta \cdot (p_x - 1) + (p_y - 1)) + y_c, \forall p_x < 1; \forall p_y < 1 \\ \frac{l}{2} \cdot \lambda \cdot (-\delta \cdot (1 - \frac{1}{p_x}) + (p_y - 1)) + y_c, \forall p_x \geq 1; \forall p_y < 1 \\ \frac{l}{2} \cdot \lambda \cdot (-\delta \cdot (p_x - 1) + (1 - \frac{1}{p_y})) + y_c, \forall p_x < 1; \forall p_y \geq 1 \\ \frac{l}{2} \cdot \lambda \cdot (-\delta \cdot (1 - \frac{1}{p_x}) + (1 - \frac{1}{p_y})) + y_c, \forall p_x \geq 1; \forall p_y \geq 1 \end{cases} \quad (4)$$

where the central point (x_c, y_c) has also been considered, as well as the aperture misalignment δ, the aperture length l and the ratio between the actual focal length h'_{ap} and the expected focal length h_{ap}, where $\lambda = \frac{h'_{ap}}{h_{ap}}$ [34] (see Fig. 3).

After the coordinates of the image points $(x_r, y_r)_i$ for each emitter i are estimated, the algorithm continues to determine the rotation γ of the receiver around the Z axis by means of trigonometric equations, based on the fact that the illuminated area on the surface of the sensor is always squared [35]. The rotation angle γ is used to rotate the image points $-\gamma$ degrees to obtain the non-rotated image points $(x'_r, y'_r)_i$. This is a necessary step since the positioning algorithm requires the receiver to be aligned with the reference frame. Then, the positioning method proceeds to estimate the receiver's coordinates (x, y, z) by using a Least Squares Estimator (LSE) and trigonometric considerations, detailed in Eqs. (5) and (6) [34]. Note that coordinate z is obtained as the weighted average considering the distances d_i between the estimated receiver' position (x, y) and the projection of each transmitter i in the plane where the receiver is placed.

$$(x, y) = (\mathbf{A}^T \cdot \mathbf{A})^{-1} \cdot \mathbf{A}^T \cdot \mathbf{b} \quad (5)$$

$$\text{Where } \mathbf{A} = \begin{bmatrix} -y'_{r,1} & x'_{r,1} \\ -y'_{r,2} & x'_{r,2} \\ -y'_{r,3} & x'_{r,3} \\ -y'_{r,4} & x'_{r,4} \end{bmatrix} \text{ and } \mathbf{b} = \begin{bmatrix} y_{t,1} \cdot x'_{r,1} - x_{t,1} \cdot y'_{r,1} \\ y_{t,2} \cdot x'_{r,2} - x_{t,2} \cdot y'_{r,2} \\ y_{t,3} \cdot x'_{r,3} - x_{t,3} \cdot y'_{r,3} \\ y_{t,4} \cdot x'_{r,4} - x_{t,4} \cdot y'_{r,4} \end{bmatrix}$$

$$z_i = z_{t,i} - h_{ap} \cdot \left(1 + \sqrt{\frac{(x_{t,i} - x)^2 + (y_{t,i} - y)^2}{x'^2_{r,i} + y'^2_{r,i}}}\right)$$

$$z = \frac{1}{\sum_{i=1}^{i} d_i^2} \cdot \sum_{i=1}^{i} \left(d_i^2 \cdot z_i\right) \quad (6)$$

B. Adopted Machine Learning Algorithms

The energy received at each frequency QD_j, for each quadrant $j = \{1, 2, 3, 4\}$, leads to an input dimensionality of 16 RSS values. However the individual RSS values are not all uncorrelated and a more efficient representation can be found by using an autoencoder [33]. An autoencoder is a type of artificial neural network that is trained to attempt to copy its input to its output. However it consists of a hidden layer which describes a code that represents the input. The network can be viewed as consisting of two parts: an encoder function and a decoder function. Due to the fact that the hidden layer has a lower dimensionality than the input layer, the network learns to prioritize certain aspects of the training data and, thus, often learns the useful properties of data. Once trained, the encoder step of the network generates an efficient and lower dimensional representation of the original input data and these features can be then used in the GP model. In this work an encoder using only feed forward network functions and with a single hidden layer is selected for dimensionality reduction. The input dimensionality of the encoder is 16 and the dimensionality of the hidden layer is 4. The hyperbolic tangent function is added as non-linear activation to the hidden layer. A schematic representation of the implemented autoencoder is presented in Fig. 4.

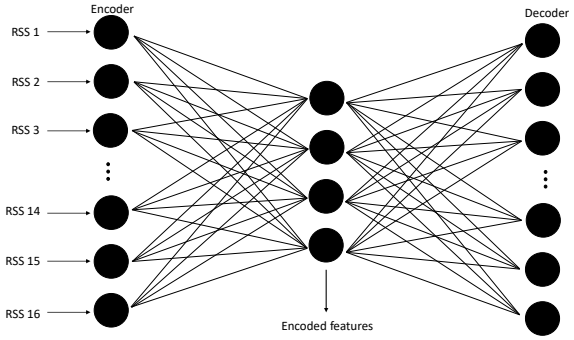

Fig. 4. A schematic representation of an autoencoder neural network.

In this context, the positioning problem is considered to be a supervised regression problem. There are many existing types of models for regression [36]–[39], however GPs feature being very data-efficient [40] and allow automatic hyperparameter optimization and regularization. A summary of the GP model and its parameters is detailed in Table III. A GP is a generalization of the Gaussian probability distribution [30], where a probability distribution describes random variables and a stochastic process governs the properties of functions [30]. More formally [30], GPs are powerful non-parametric Bayesian models defined by a kernel function $k(\mathbf{x}, \mathbf{x}')$ and a mean function $\rho(\mathbf{x})$, such that the probability of

any finite set of input-output pairs $\{(\mathbf{x}_i, f_i)\}_{i=1}^N$ is distributed according to a Gaussian distribution with a mean $[\rho(\mathbf{x}_i)]_{i=1}^N$ and a covariance K. In this work, $\mathbf{x}_i$ are vectors containing the RSS input features and f_i are the Euclidean coordinates. Each entry of the covariance matrix is defined by $K_{ij} = k(\mathbf{x}_i, \mathbf{x}_j)$. The mean function is considered to be zero.

The chosen kernel function is the Radial Basis Function [30]:

$$k(\mathbf{x}, \mathbf{x}') = \sigma_k^2 \exp\left(\frac{\|\mathbf{x} - \mathbf{x}'\|^2}{2\ell_p^2}\right). \tag{7}$$

The hyperparameters $\zeta = \{\sigma_k, \ell_p\}$ are optimized by maximizing the log likelihood of the data [30]:

$$\hat{\zeta} = \arg\max_{\zeta} \log p(\mathbf{f}|\zeta) \tag{8}$$

$$= \arg\max_{\zeta} -\frac{1}{2}\left(\log|2\pi K| + \mathbf{f}^T K^{-1}\mathbf{f}\right) \tag{9}$$

A prediction for a new input $\mathbf{x}_\star$ is obtained by computing the conditional distribution, resulting in a Gaussian distribution with mean $k_\star^T K^{-1}\mathbf{f}$ and covariance $k_{\star\star} - k_\star^T K^{-1} k_\star^T$, where:

$$(k_\star)_i = k(\mathbf{x}_\star, \mathbf{x}_i), \tag{10}$$

$$k_{\star\star} = k(\mathbf{x}_\star, \mathbf{x}_\star). \tag{11}$$

TABLE III
SUMMARY OF THE GP MODEL AND ITS PARAMETERS

System parameters	Parameter value
Mean function $\rho(\mathbf{x})$	Chosen to be zero
Kernel function $k(\mathbf{x}, \mathbf{x}')$	Radial Basis Function
Training set sizes N	{40, 50, 75}
Training method	20-fold cross validation
Number of inputs	4
Complexity	$\mathcal{O}(N^3)$
Kernel Hyperparameters	
Characteristic length-scale ℓ_p	Optimized during training phase
Signal variance σ_k	Optimized during training phase

IV. EXPERIMENTAL RESULTS

The experimental tests have been carried out in an area of 3×3 m^2 with a height of 1.3 m, under normal light conditions. Four visible light LEDs have been placed in the ceiling of the test area, at the four corners of a rectangle of 1.35 m $\times$ 1.9 m, as depicted in Fig. 5. The deployed LEDs are an individual Chip On Board (COB) LED Bridgelux BXRE-C3001-D24. Each LED $i = \{1, 2, 3, 4\}$ has its unique central frequency $f = \{500, 1000, 2000, 4000\}$ Hz, respectively. Note that since the aperture height is set at $h_{ap} = 2.5$ mm, and the length of the quadrant photodiode is $l = 10$ mm, the FoV of the receiver is $FoV = \tan^{-1}\left(\frac{l/2}{h_{ap}}\right) \cdot 2 = \tan^{-1}\left(\frac{5}{2.5}\right) \cdot 2 = 63.43 \cdot 2 = 126.87°$. That means that, with a transmitters' height of $H = 1.3$ m, the receiver can move, in plane XY, up to $d = H \cdot \tan(FOV/2) = 1.3 \cdot \tan(63.43°) = 2.60$ m far away from the projection of a LED and still receives signal from it. Taking that into account, all the experimental tests are within the coverage of the four transmitters.

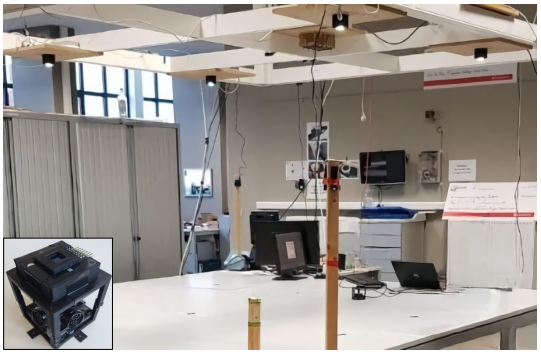

Fig. 5. View of the experimental setup in the proposed scenario with the four transmitting LEDs. A close-up of the quadrant photodiode receiver and Marvelmind ground-truth mobile node is detailed in the bottom-left corner.

The reception system consists of: 1) a quadrant photoreceptor Hamamatsu S5981 plus a 10 mm long square aperture placed over it in such a way that the incident signal passes through the aperture and illuminates part of its surface (see Fig. 6); 2) an external crystal oscillator; and 3) a National Instruments USB-6215 acquisition system connected to a computer via USB, where the detected signals are processed. The acquisition frequency is set at 128 kHz.

In addition, a highly accurate ultrasound localization system Super-NIA-3D Marvelmind Robotics has been used to obtain the ground-truth (real positions) of the receiver and the transmitting beacons. The Marvelmind ultrasound system and the VLP receiver provide synchronized measurement updates.

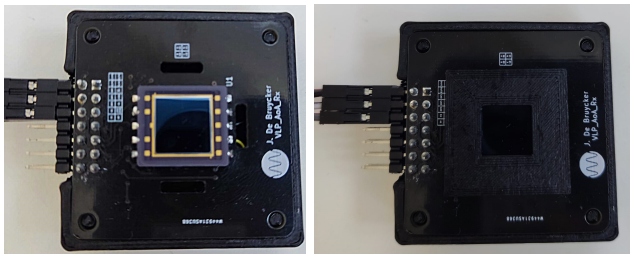

(a) (b)

Fig. 6. Quadrant photodiode a) without aperture, b) with aperture.

To evaluate the VLP's performance, multiple experimental points were collected by randomly moving the receiver in the test area, both inside and outside the rectangle formed by the LED projections in the XY plane. Fig. 7 shows a top view of the acquired dataset, consisting of 110 non-overlapping data points with an interdistance of at least 5 cm.

With regard to the AoA algorithm, the calibration parameters in Eqs. (3)-(4) are estimated using 70% of the acquired dataset. The parameters are set at $\delta = 0.1$ rad, $(x_c, y_c) = (0.05, 0.05)$ mm, $l = 10$ mm, $h_{ap} = 2.5$ mm, and $\lambda = 0.92$. In case of the data-driven approach, the acquired dataset is preprocessed by computing the natural logarithm of the RSS values and then applying a standard scaler to the resulting values. These scaled RSS vectors are then used to train the autoencoder model in order to facilitate dimensionality reduction and feature extraction. Next, a GP model is trained with varying training set sizes of $N = \{40, 50, 75\}$

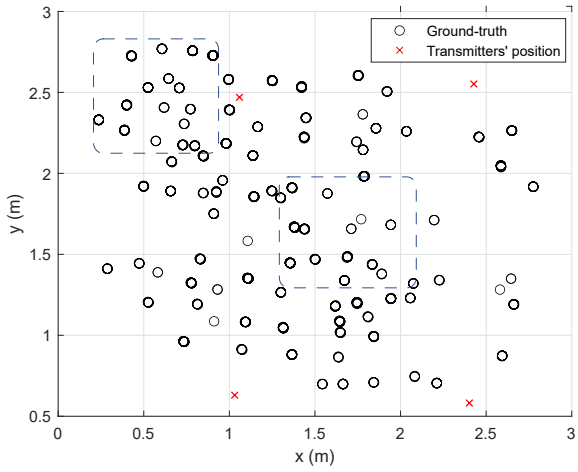

Fig. 7. Top view of the dataset acquired in the experimental setup, location of the transmitters and test scenarios. Globally, 110 non-overlapping points were measured.

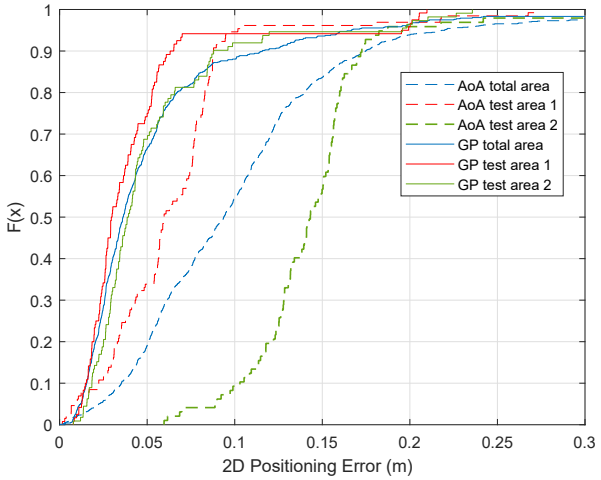

Fig. 8. CDF of the global 2D absolute error using AoA and ML techniques whether $N = 75$.

with the resulting feature vectors. Because of the limited size (110) of the total dataset, a cross validation strategy using 20 independent train-test splits for every training set size N is evaluated to obtain statistically relevant results. The performance of the model is only evaluated on the test portions of the dataset. Furthermore, the model trained with $N = 75$ is also evaluated on the entire dataset of 1700 data points, which thus contains many overlapping measurements, with the objective of evaluating the precision of the model and RSS-based method.

The Cumulative Distribution Function (CDF) of the positioning error for the AoA and ML techniques are shown in Fig. 8 and the p50 and p95 values are presented in Table IV. The metric used to assess positioning accuracy is the Euclidean distance error E_d of the estimate with respect to the ground-truth (12), where (x, y) are the ground-truth coordinates and $(\widehat{x}, \widehat{y})$ are the estimated positions.

$$E_d = \sqrt{(\widehat{x} - x)^2 + (\widehat{y} - y)^2} \tag{12}$$

It is worth noting that, although the AoA-based triangulation approach detects the location of the receiver and its rotation γ on the Z axis (x, y, z, γ), for the sake of comparison with the GP regression, in Fig. 8 and Table IV, only the 2D coordinates are presented. In the entire area, the experimental tests achieve p50 and p95 2D absolute errors below 9.4 cm and 21.9 cm for the AoA-based triangulation algorithm, and 3.6 cm and 16.6 cm for the Gaussian Process in the case $N = 75$. The 3D p50 absolute errors for the AoA-based triangulation approach are below 6.7 cm, 14.6 cm and 10.1 cm for the test area 1, test area 2 and the total area, respectively.

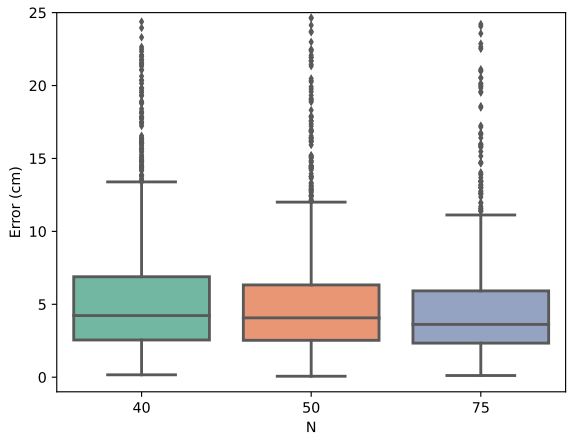

Fig. 9. Error distribution of the approach using GP regression according to the different training set sizes.

TABLE IV
P50 AND P95 VALUES OF THE CDF, AVERAGE AND MAXIMUM ERRORS FOR THE 2D POSITIONING ERROR USING AOA AND ML TECHNIQUES.

	Method	p50 (cm)	p95 (cm)	Average error (cm)	Maximum error (cm)
Test area 1	AoA	5.97	9.49	6.44	27.28
	GP	2.30	12.40	4.30	20.98
Test area 2	AoA	14.32	18.56	14.37	33.45
	GP	3.36	10.35	5.23	23.57
Total area	AoA	9.38	21.94	10.20	55.89
	GP	3.62	16.65	5.46	47.15

In Fig. 9, the corresponding boxplots are shown of the positioning error distribution of the GP model according to the considered training set sizes. From this figure it can be observed that, even for the smallest training set size, the GP model achieves a p50 error well below 5 cm in the considered experimental setup. The p95 error reduces as training set size does, and it is below 18 cm for all the considered scenarios. When the GP model trained with $N = 75$ points is evaluated on the entire set of 1700 data points, a p50 error of 3.09 cm and p95 error of 21.4 cm are found.

From Table IV it can be derived that the ML method provides more accurate results in general, most notably in terms of p50 error but also for the p95 errors, than the analytical AoA method. Furthermore when focusing on the two distinct test areas, it is possible to observe that the GP model slightly outperforms the AoA method in the center in terms of p50 error but reports a higher p95 error on the considered locations there. As for the test area at the corner of

the experimental setup, the GP model clearly outperforms the analytical AoA method in terms of both p50 and p95 errors.

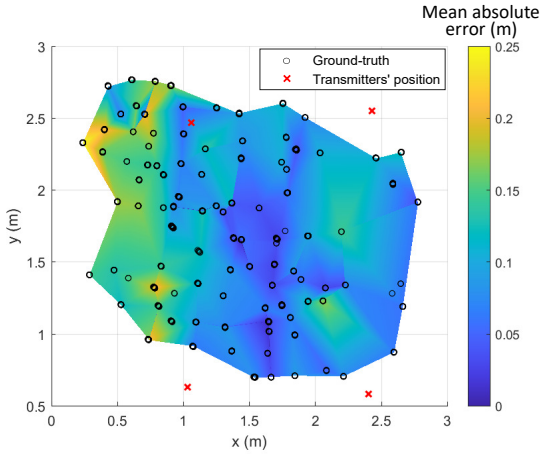

(a)

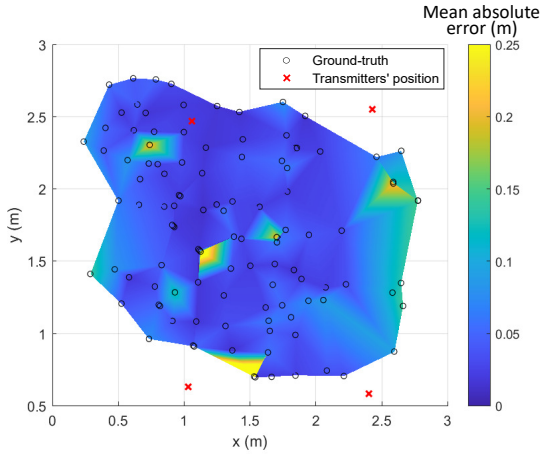

(b)

Fig. 10. Average 2D positioning errors at each testing location using: a) AoA method; b) GP method.

For clarity's sake, a colour map of the obtained 2D average positioning errors at each position is presented in Fig. 10, using the AoA and the GP methods. Note that the AoA method performs better in the centre of the test area compared to the corner of the room, since, although those points are within the coverage area of the VLPS, some LEDs may not be clearly detected by the receiver and its RSS values may not be accurate enough (due to frequency leaking, high incident angles, miscalibrated parameters, etc.). A solution to improve its performance is to implement encoding techniques in the emission of the LEDs and increase the feasible distance between the transmitters and the receiver [34]. The fact that the analytical AoA approach needs accurate RSS values is a disadvantage in comparison with the GP model.

In addition, it is worth noting that the analytical AoA method can also provide 3D location estimates without requiring additional training data. In order to facilitate 3D positioning, the used GP model would require observed or simulated data at different z-coordinates, which complicates the training process. This is a clear disadvantage in comparison with the analytical AoA method.

Although the initial application considered here (e.g., the guidance of a mobile robot in the floor) only involves the rotation γ around the vertical axis Z (i.e., getting always $\alpha = \beta = 0°$), whether rotations around the X and Y axes are considered, the following considerations apply:

- ML algorithms are not sensitive to a rotation on the Z axis since they always consider the global received energy, which does not depend on this rotation. In addition, if rotations around the X and Y axes are taken into account, ML algorithms should be trained for those situations, what is beyond the scope of this work.
- Triangulation-based algorithms can be analysed for errors derived from possible rotations around the X and Y axes. By means of simulation, the errors obtained for cases with small rotations (up to $5°$) in the X, Y and both axes have been determined. Note that rotations around the Z axis have already been estimated by the proposed algorithm.

Fig. 11 shows the CDF of the absolute error when the receiver is located every 20 cm on a grid of 3.5×3 m^2 for small rotations in the X and Y axes. The output signals of the quadrant photoreceiver present a 10 dB Signal-to-Noise ratio. The LED's coordinates are provided in Table II and 20 iterations are carried out for each location. According to the CDF, for the 90% of cases, the 2D positioning error is below 5 cm if there is no rotation around X or Y; below 30 cm if there is a $5°$ rotation in any axis (X or Y); and about 45 cm if the rotation is $5°$ in α and β (both X and Y axes).

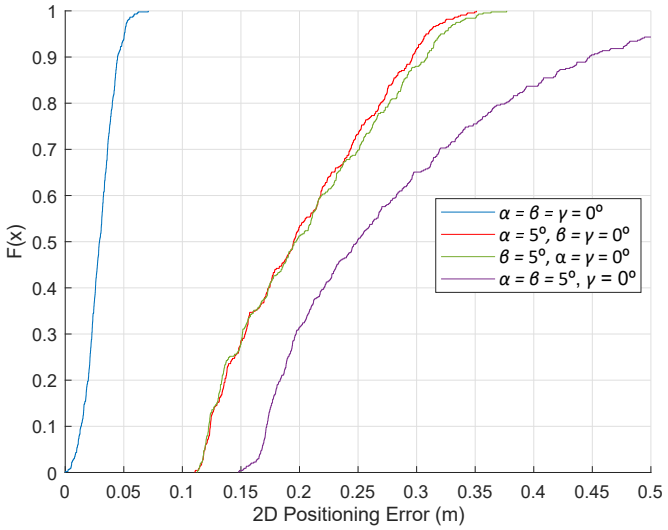

Fig. 11. CDF of the absolute 2D positioning error using the AoA method when tilting the receiver up to $5°$ in the X, Y and both axes.

V. Conclusions

In this work an experimental evaluation of the performance achieved by Gaussian Processes for 2D visible light positioning is assessed when using a quadrant photodiode and an aperture as receiver sensor. The data-driven GP method is compared to an analytical AoA multilateration-based method, which uses the same receiver hardware. From the conducted experiments and results, it can be concluded that the data-driven method delivers more robust and accurate positioning

in the 2D case. When evaluated over the entire area, the AoA method achieves a p50 error of $9.38\,\text{cm}$ and a p95 error of $21.94\,\text{cm}$, whereas the GP model obtains a p50 error of $3.62\,\text{cm}$ and a p95 error of $16.65\,\text{cm}$. Another important conclusion is that the GP is capable of delivering robust results in the test area 2 (corner of the setup) with a p50 error of $3.36\,\text{cm}$ and a p95 error of $10.35\,\text{cm}$, whereas the p50 and p95 errors for the analytical method are $14.32\,\text{cm}$ and $18.56\,\text{cm}$, respectively, in that area. Finally, the analytical method can provide 3D positioning without requiring additional training data, while the GP model would require additional observations at different z-coordinates to achieve this.

REFERENCES

[1] J. Schiller and A. Voisard, *Location-Based Services*. The Morgan Kaufmann Series in Data Management Systems, Elsevier Science, 2004.

[2] P. Puricer and P. Kovar, "Technical Limitations of GNSS Receivers in Indoor Positioning," in *17th Inter. Conf. Radioelektronika*, pp. 1–5, 2007.

[3] D. Gualda, M. C. Pérez-Rubio, J. Ureña, S. Pérez-Bachiller, J. M. Villadangos, Á. Hernández, J. J. García, and A. Jiménez, "LOCATE-US: Indoor Positioning for Mobile Devices Using Encoded Ultrasonic Signals, Inertial Sensors and Graph-Matching," *Sensors*, vol. 21, no. 6, 2021.

[4] J. K. Lee and W. Jung, "Vertical Position Estimation of a Constrained Link Using IMU Signals and Kinematic Constraint," *2018 IEEE SENSORS*, pp. 1–4, 2018.

[5] A. Poulose, Emeršič, O. Steven Eyobu, and D. Seog Han, "An Accurate Indoor User Position Estimator For Multiple Anchor UWB Localization," in *2020 International Conference on Information and Communication Technology Convergence (ICTC)*, pp. 478–482, 2020.

[6] J. C. Torres, A. Montes, S. L. Mendoza, P. R. Fernández, J. S. Betancourt, L. Escandell, C. I. del Valle, and J. M. Sánchez-Pena, "A Low-Cost Visible Light Positioning System for Indoor Positioning," *Sensors*, vol. 20, no. 18, 2020.

[7] H. Li, H. Huang, Y. Xu, Z. Wei, S. Yuan, P. Lin, H. Wu, W. Lei, J. Fang, and Z. Chen, "A Fast and High-Accuracy Real-Time Visible Light Positioning System Based on Single LED Lamp With a Beacon," *IEEE Photonics Journal*, vol. 12, no. 6, pp. 1–12, 2020.

[8] E. Bernardes, S. Viollet, and T. Raharijaona, "A Three-Photo-Detector Optical Sensor Accurately Localizes a Mobile Robot Indoors by Using Two Infrared Light-Emitting Diodes," *IEEE Access*, vol. 8, pp. 87490–87503, 2020.

[9] C. Wang, L. Wang, X. Chi, S. Liu, W. Shi, and J. Deng, "The research of indoor positioning based on visible light communication," *China Communications*, vol. 12, no. 8, pp. 85–92, 2015.

[10] S. Cincotta, C. He, A. Neild, and J. Armstrong, "Indoor visible light positioning: Overcoming the practical limitations of the quadrant angular diversity aperture receiver (QADA) by using the two-stage QADA-plus receiver," *Sensors (Switzerland)*, vol. vol. 19, no. 4, 2019.

[11] X. Guo, J. Liu, Y. Bai, L. Zhu, K. Zhang, and Y. Liu, "Photodiode array-based angular estimator and it's application in indoor positioning with single led lamp," in *Asia Commu. and Photonics Conf. and Inter. Conf. on Information Photonics and Optical Commu.*, pp. 1–3, 2020.

[12] B. Zhu, Z. Zhu, Y. Wang, and J. Cheng, "Optimal optical omnidirectional angle-of-arrival estimator with complementary photodiodes," *Journal of Lightwave Technology*, vol. vol. 37, no. 13, pp. 2932–2945, 2019.

[13] E. Aparicio-Esteve, Á. Hernández, J. Ureña, J. M. Villadangos, S. Lluva, and M. C. Pérez-Rubio, "Detecting Relative Amplitude of IR Signals with Active Sensors and Its Application to a Positioning System," *Applied Sciences*, vol. vol. 10, no. 18, pp. 1–12, 2020.

[14] S. Cincotta, C. He, A. Neild, and J. Armstrong, "High angular resolution visible light positioning using a quadrant photodiode angular diversity aperture receiver (QADA)," *Optics Express*, vol. 26, no. 7, pp. 9230–9242, 2018.

[15] Á. De la Llana Calvo, *Contribución al Posicionamiento en Interiores Basado en Emisores de Señal Óptica y Detectores PSD*. PhD thesis, Universidad de Alcalá, 2020.

[16] Á. De-La-Llana-Calvo, J.-L. Lázaro-Galilea, A. Gardel-Vicente, D. Salido-Monzú, I. Bravo-Muñoz, A. Iamnitchi, and R. Gil-Vera, "Weak Calibration of a Visible Light Positioning System Based on a Position-Sensitive Detector: Positioning Error Assessment," *Sensors*, vol. vol. 21, no. 11, 2021.

[17] N. Stevens, "Bias Introduced by True Radiation Patterns in RSS-based Visible Light Positioning," in *2019 IEEE SENSORS*, pp. 1–4, 2019.

[18] C. Danakis, M. Afgani, G. Povey, I. Underwood, and H. Haas, "Using a CMOS camera sensor for visible light communication," in *2012 IEEE Globecom Workshops*, pp. 1244–1248, 2012.

[19] H. Steendam, T. Q. Wang, and J. Armstrong, "Theoretical Lower Bound for Indoor Visible Light Positioning Using Received Signal Strength Measurements and an Aperture-Based Receiver," *Journal of Lightwave Technology*, vol. 35, no. 2, pp. 309–319, 2017.

[20] A. Nessa, B. Adhikari, F. Hussain, and X. N. Fernando, "A Survey of Machine Learning for Indoor Positioning," *IEEE Access*, vol. 8, pp. 214945–214965, 2020.

[21] H. Zhang, J. Cui, L. Feng, A. Yang, H. Lv, B. Lin, and H. Huang, "High-Precision Indoor Visible Light Positioning Using Deep Neural Network Based on the Bayesian Regularization With Sparse Training Point," *IEEE Photonics Journal*, vol. 11, pp. 1–10, June 2019.

[22] S. Zhang, P. Du, C. Chen, W. Zhong, and A. Alphones, "Robust 3D Indoor VLP System Based on ANN Using Hybrid RSS/PDOA," *IEEE Access*, vol. 7, pp. 47769–47780, 2019.

[23] M. Ramadan, V. Sark, J. Gutierrez, and E. Grass, "NLOS identification for indoor localization using random forest algorithm," in *WSA 22nd International ITG Workshop on Smart Antennas*, pp. 1–5, VDE, 2018.

[24] H. Wymeersch, S. Maranò, W. M. Gifford, and M. Z. Win, "A machine learning approach to ranging error mitigation for UWB localization," *IEEE Trans. on communications*, vol. 60, no. 6, pp. 1719–1728, 2012.

[25] C.-Y. Hong, Y.-C. Wu, Y. Liu, C.-W. Chow, C.-H. Yeh, K.-L. Hsu, D.-C. Lin, X.-L. Liao, K.-H. Lin, and Y.-Y. Chen, "Angle-of-Arrival (AOA) Visible Light Positioning (VLP) System Using Solar Cells With Third-Order Regression and Ridge Regression Algorithms," *IEEE Photonics Journal*, vol. 12, no. 3, pp. 1–5, 2020.

[26] C.-Y. Hong, Y. Wu, Y. Liu, K.-L. Hsu, W. H. Gunawan, A. Adnan, L.-Y. Wei, C.-H. Yeh, and C.-W. Chow, "Using silicon photovoltaic cells and machine learning and neural network algorithms for visible-light positioning systems," *Optical Engin.*, vol. 59, no. 9, pp. 1 – 8, 2020.

[27] H. Steendam, "A 3-d positioning algorithm for aoa-based vlp with an aperture-based receiver," *IEEE Journal on Selected Areas in Communications*, vol. 36, no. 1, pp. 23–33, 2018.

[28] H. Hosseinianfar and M. Brandt-Pearce, "Performance Limits for Fingerprinting-Based Indoor Optical Communication Positioning Systems Exploiting Multipath Reflections," *IEEE Photonics Journal*, vol. 12, no. 4, pp. 1–16, 2020.

[29] S. Shen, S. Li, and H. Steendam, "Simultaneous Position and Orientation Estimation for Visible Light Systems With Multiple LEDs and Multiple PDs," *IEEE Journal on Selected Areas in Communications*, vol. 38, no. 8, pp. 1866–1879, 2020.

[30] C. E. Rasmussen and C. K. Williams, *Gaussian Processes for Machine Learning*. University Press Group Limited, 2006.

[31] R. B. Langley, "Dilution of precision," 1999.

[32] W. Zhang, W. Guo, C. Zhang, and S. Zhao, "An Improved Method for Spot Position Detection of a Laser Tracking and Positioning System Based on a Four-Quadrant Detector," *Sensors*, vol. 19, no. 21, 2019.

[33] I. Goodfellow, Y. Bengio, and A. Courville, *Deep Learning*. MIT Press, 2016.

[34] E. Aparicio-Esteve, Á. Hernández, and J. Ureña, "Design, Calibration, and Evaluation of a Long-Range 3-D Infrared Positioning System Based on Encoding Techniques," *IEEE Transactions on Instrumentation and Measurement*, vol. 70, pp. 1–13, 2021.

[35] E. Aparicio-Esteve, Á. Hernández, J. Ureña, J. M. Villadangos, and F. Ciudad, "Estimation of the Polar Angle in a 3D Infrared Indoor Positioning System based on a QADA receiver," in *International Conference on Indoor Positioning and Indoor Navigation*, pp. 1–8, 2019.

[36] D. Fonseca, D. Navaresse, and G. Moynihan, "Simulation metamodeling through artificial neural networks," *Engineering Applications of Artificial Intelligence*, vol. 16, no. 3, pp. 177–183, 2003.

[37] T. J. Santner, B. J. Williams, and W. I. Notz, *The design and analysis of computer experiments*. Springer Science & Business Media, 2013.

[38] D. Gorissen, I. Couckuyt, P. Demeester, T. Dhaene, and K. Crombecq, "A surrogate modeling and adaptive sampling toolbox for computer based design," *Journal of Machine Learning Research*, vol. 11, pp. 2051–2055, 2010.

[39] J. A. K. Suykens and J. Vandewalle, "Least Squares Support Vector Machine Classifiers," *Neural Process. Lett.*, vol. 9, no. 3, pp. 293–300, 1999.

[40] N. Knudde, W. Raes, J. De Bruycker, T. Dhaene, and N. Stevens, "Data-Efficient Gaussian Process Regression for Accurate Visible Light Positioning," *IEEE Comm. Letters*, vol. 24, no. 8, pp. 1705–1709, 2020.